ELSEVIER

Nuclear Instruments and Methods in Physics Research A 439 (2000) 91–110

NUCLEAR INSTRUMENTS & METHODS IN PHYSICS RESEARCH Section A

www.elsevier.nl/locate/nima

A polarized ^{3}He internal target for storage rings

H.R. Poolman[a,b,*], J.F.J. van den Brand[a,b], H.J. Bulten[a,b], M. Doets[b], R. Ent[c], M. Ferro-Luzzi[a,b], D.G. Geurts[a], M. Harvey[c], F.A. Mul[a]

[a]*Faculty of Sciences/Division of Physics and Astronomy, Vrije Universiteit, 1081 HV Amsterdam, The Netherlands*
[b]*National Institute for Nuclear Physics and High Energy Physics, P.O. Box 41882, 1009 DB Amsterdam, The Netherlands*
[c]*Department of Physics, Hampton University, Hampton, VA 23668, USA*

Received 12 August 1999; accepted 12 August 1999

Abstract

A polarized ^{3}He internal target was employed at the internal target facility of the Amsterdam electron Pulse Stretcher and Storage ring (AmPS) at the Dutch National Institute for Nuclear and High-Energy Physics (NIKHEF). The unique features of internal targets such as chemical and isotopic purity, high and rapidly reversible polarization, and the ability to manipulate the target spin orientation were successfully demonstrated. A nuclear polarization of 0.50 (0.42) at a ^{3}He gas flow of 1.0 (2.0) $\times 10^{17}$ at s^{-1} could be obtained. Operation at a nominal flow of 1×10^{17} at s^{-1} resulted in a target thickness of 0.7×10^{15} at cm^{-2} at a target temperature of 17 K.

PACS: 67.65. + z; 29.25.Pj; 29.20. − c

Keywords: Polarized ^{3}He; Internal target; Storage ring

1. Introduction

In the scattering of leptons from hadronic targets the leptonic part of the interaction is presumed to be well understood from quantum electrodynamics, thereby studies can be focussed on the strong-interaction vertex and the underlying structure and dynamics of the nucleus. The ultimate probe consists of fully spin-dependent scattering with polarized leptons and polarized targets [1], and the last decade has seen a large effort devoted to the realization of such experiments. Spin-dependent quasifree electron scattering from ^{3}He can increase our knowledge of the components of the nuclear and nucleon wave functions. Access to the small amplitudes of the ^{3}He ground-state wave function is enhanced as they enter the spin observables through interference terms with larger and consequently better known scattering amplitudes.

It is generally believed that polarized ^{3}He ($\overrightarrow{^3\mathrm{He}}$) can serve as an effective polarized neutron target. Several experiments have been initiated along this line of reasoning in both nuclear [2,3] and particle [4] physics. Important results on the neutron form factors and deep-inelastic structure functions have been obtained (see, e.g. Refs. [5–8]) in recent experiments. In order to achieve adequate luminosity,

* Corresponding author. Tel.: + 31-20-444-7906; fax: + 31-20-444-7999.

E-mail address: hansrp@nat.vu.nl (H.R. Poolman)

0168-9002/00/$ - see front matter
PII: S0168-9002(99)00861-X

these experiments utilize electron beams impinging on external polarized targets. Although typically lower in luminosity, spin-dependent electron scattering experiments from polarized gas targets internal to storage rings have the advantage that (i) they can be well matched to the application of large-acceptance detectors; (ii) rapid polarization reversal and flexible orientation of the nuclear target spin can be obtained, reducing systematic uncertainties; and (iii) low-energy recoiling particles can escape the ultra-thin targets and be detected. In such an experiment a source injects (polarized) atoms into a storage cell through which the stored electron beam passes. So far, electronuclear spin observables from experiments with internal polarized gas targets and polarized leptons have been obtained only at DESY [4] in the deep-inelastic scattering regime.

This paper describes the first polarized ^{3}He internal target that was employed in a medium-energy electron storage ring [3,9]. The main features of this experiment are described in Sections 2 and 3, together with the novel technique of injecting and storing polarized electrons in a medium-energy electron storage ring. In Sections 4 and 5 a detailed description is given of the principle and performance of the polarized ^{3}He target.

2. Experimental setup

2.1. Introduction

The experiment was performed in the internal target hall (ITH) of the Amsterdam Pulse Stretcher (AmPS) storage ring facility at NIKHEF [10]. Fig. 1 shows an overview of AmPS and the location of the main components relevant for a spin-dependent electron scattering experiment, e.g. the polarized electron source, Siberian snake, Compton backscattering polarimeter (CBP), and polarized internal target. The polarized electron source (PES) is the result of a collaboration between NIKHEF, the Budker Institute for Nuclear Physics (BINP) and the Institute of Semiconductor Physics (ISP) in Novosibirsk. Electron bunches are injected into AmPS from the linear medium-energy accelerator (MEA) with energies up to 770 MeV.

The characteristic time for self-polarization of a stored electron beam due to emission of synchrotron radiation through the Sokolov–Ternov effect [11] is given by $\tau_p \approx 100\rho^2 R/E_b^5$ (in s), where ρ is the magnetic bending radius and R the geometric radius of the storage ring (in m) and E_b the electron energy (in GeV). For AmPS, with electron energies below 1 GeV the self-polarizing time is too long

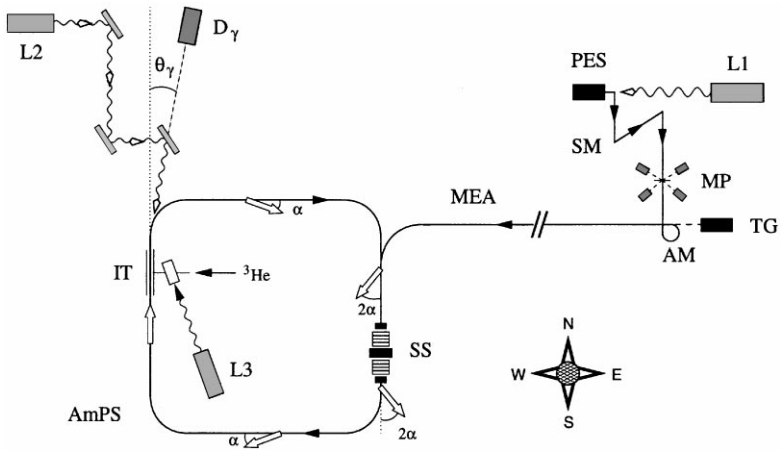

Fig. 1. Overview of the AmPS storage ring at NIKHEF showing the polarized electron source (PES), spin manipulator (SM), Mott polarimeter (MP), thermionic gun (TG), alpha magnet (AM), linear accelerator (MEA), Siberian snake (SS), CBP photon detector (D_γ), and internal target (IT). Lasers are indicated with L1, L2 and L3. The stable in-plane polarization direction for stored electrons with the full snake on is illustrated.

($\tau_p \geq 2.5 \times 10^4$ s) compared to typical beam lifetimes ($\tau_b \approx 2 \times 10^3$ s), to take advantage of in a scattering experiment. Therefore, one has to inject longitudinally polarized electrons into the storage ring and use Siberian snake techniques to preserve the polarization. In order to monitor the beam polarization at the IT a Compton backscattering polarimeter was constructed [12].

3. Detector system

The experiments were performed with a large acceptance detector setup. Scattered electrons were detected in the *Bigbite* magnetic spectrometer consisting of a wedge-shaped dipole magnet with a gap of 250 mm and an effective length of 600 mm, two sets of drift chambers, a scintillator hodoscope, and an aerogel Cherenkov detector. The spectrometer had a momentum resolution of 1% and a momentum acceptance exceeding 50% [13]. Knocked-out protons and deuterons were measured in a range telescope [14] with a solid angle of 180 msr and an energy resolution of approximately 3% (FWHM). The range telescope consisted of sixteen layers of plastic scintillator (NE102) each with an area of $30 \times 50\,\text{cm}^2$ and a thickness of 10 mm. A neutron detector, consisting of eight telescopes arranged in two walls of $160 \times 80\,\text{cm}^2$ front surface measured the knocked-out neutrons by the time-of-flight method. Each telescope consisted of three layers of scintillator, the first 3 mm thick, the second 10 mm thick, and the third 200 mm thick. Each scintillator had a double-sided readout by photo-multiplier tubes (PMT). A neutron was selected as a coincidence between the two PMTs on the 200 mm thick bars and a 8–12 fold veto by all surrounding scintillators. Each wall covered approximately 200 msr and had a neutron detection efficiency of about 20%. Recoiling hadrons were detected with a silicon-strip detector [15] located in a secondary vacuum system. It consists of two arrays of three silicon strip detectors each and a plastic scintillator of 5 mm thickness. This detector mounts onto the scattering chamber at a fixed angle $\theta_{\text{rec}} = 70^\circ$ and less than 20 cm from the internal target cell. It allows for clean detection of low-energy target fragments (p, d, ^{3}H, ^{3}He) [16] by keeping the amount of material between the target and detector to a minimum.

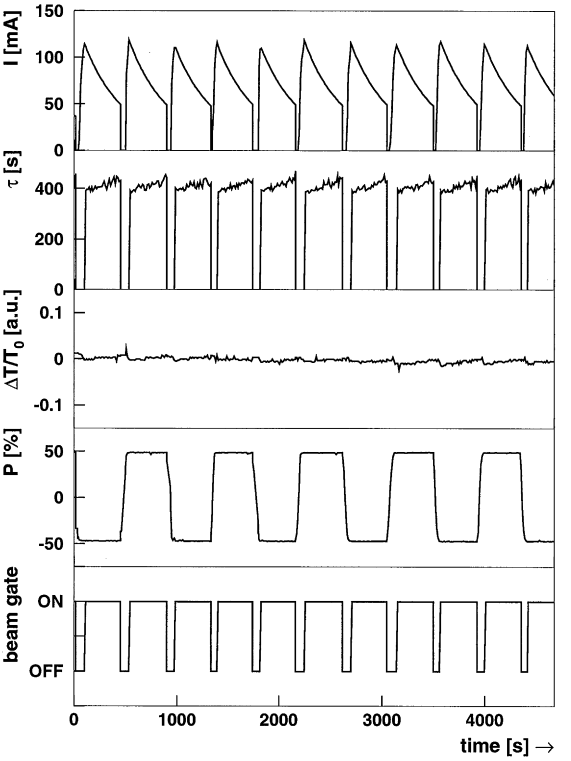

Fig. 2. An overview of the data acquisition sequence as a function of time. The top two graphs show the electron beam current and lifetime during each fill. The relative target temperature is shown in the middle graph. The bottom two graphs show the reversal of the target spin and the status (ON/OFF) of the data acquisition beamgate.

Fig. 2 shows the beam current and lifetime, target temperature and polarization, and the data acquisition *beam gate* as a function of time during a typical data-taking sequence. It shows that a beam current in excess of 110 mA can be injected (via stacking) into the storage ring in approximately 30 s and is stored with a lifetime of about 400 s. Each segment in Fig. 2 between consecutive injections is called a *fill*. After approximately 350 s the beam current has decreased to ≤ 50 mA; the beam gate is switched OFF to pause data taking and the detector voltages are ramped down. When the wire chamber voltages are set at a value to protect them from injection flashes the polarized electron

beam is dumped to prevent that long-term spin relaxation effects in the beam result in an unknown electron polarization. The ring is filled again and when the electron beam has damped to its closed orbit each detector high voltage is ramped up to its nominal value and the beam gate is switched ON to (re-)start data taking.

For asymmetry measurements, it is essential either to monitor the relative luminosity precisely or to keep the luminosity the same for both polarization states. The relative luminosity directly depends on the ^{3}He gas flow, the electron beam current and the storage cell temperature ($\sim T^{-1/2}$). The gas flow is set at a constant value (see Section 5.3) and the beam current is continuously monitored. Fig. 2 shows that the relative target temperature and is stable within 2% during a run. It takes approximately 25 s before the polarization has reached its maximum value. The target polarization was reversed during each injection.

4. Polarization of the ^{3}He nucleus

For polarized ^{3}He internal target experiments metastability exchange optical pumping is considered to be the most suitable technique, since it provides a chemically pure target at a continuous flow. In this section the design considerations and the underlying physics principles of a polarized ^{3}He internal target are described. Three important aspects of developing a polarized internal target system are the optimization of the optical pumping process, reduction of polarization relaxation effects and the monitoring of the polarization.

4.1. Introduction

The level scheme of the helium atom can be separated in a triplet (orthohelium) and a singlet (parahelium) part. The ground state is a singlet state, given by the $1\,s^2$ configuration. The excited states are denoted by $1snl^{2S+1}L$, with $S=0$ and $S=1$ for the singlet and triplet states, respectively. The $1s2s^{2S+1}S$ states are the lowest excited states and are metastable, respectively with a lifetime of 2×10^{-2} s for the singlet state and 8×10^{3} s for the triplet state.

In radiative dipole transitions only one electron makes a change of state, to a good approximation. When both electrons (total angular momentum J) of a ^{3}He atom are excited, the energy of each state lies above that of the ground state of a He^+-ion (*auto-ionization*). The possible transitions of the electron are subject to selection rules for electric dipole transition. These selection rules are: (i) Parity changes; (ii) $\Delta L = \pm 1$; (iii) $\Delta J = 0, \pm 1$; (iv) $\Delta m_J = 0, \pm 1$; (v) $\Delta S = 0$ and (vi) $J = 0 \rightarrow J = 0$ is forbidden. The selection rule $\Delta S = 0$ shows that the ortho states and the para states of helium are optically disconnected [17]. Higher-order transitions can still take place, but the strength of the magnetic dipole or the electric quadrupole transition relative to the electric dipole transition are of order $(\alpha Z)^2$:1 and therefore negligible in the optical pumping scheme.

For isotopes with a non-zero nuclear magnetic moment the interaction with valence electrons produces an additional splitting. In contrast to the ^{4}He nucleus the ^{3}He nucleus has a spin of $\frac{1}{2}\hbar$ and a magnetic moment of $\mu_I = -2.128\mu_N$, with μ_N the nuclear magneton. Hence, ^{3}He will exhibit hyperfine structure and the interaction of μ_I with the magnetic field produced by the electrons at the position of the nucleus needs to be taken into account. The ordering of a hyperfine multiplet is not given by a unique interval rule. An early study by Fred et al. [18] of the spectrum of ^{3}He already showed that for the ^{3}P and ^{3}D states the hyperfine splitting is of the same order of magnitude as the fine structure. The most accurate calculations indeed treat the fine structure and the hyperfine structure as simultaneous perturbations. For the singlet states the hyperfine splitting is small compared to that of the triplet states. The S-states of orthohelium are split in hyperfine doublets with $F=\frac{1}{2}$ and $F=\frac{3}{2}$ and the ^{3}P states in seven hyperfine components, three with total angular momentum $F=1/2$, three with $F=3/2$ and one with $F=5/2$. The most recent study of Prestage et al. [19] of the hyperfine structure of the two lowest triplet levels of ^{3}He resulted in an agreement between theory and experiment of about 1×10^{-5}. The results of the measured hyperfine splitting of the 2^3S and 2^3P, as shown in Fig. 3, are taken from Ref. [20].

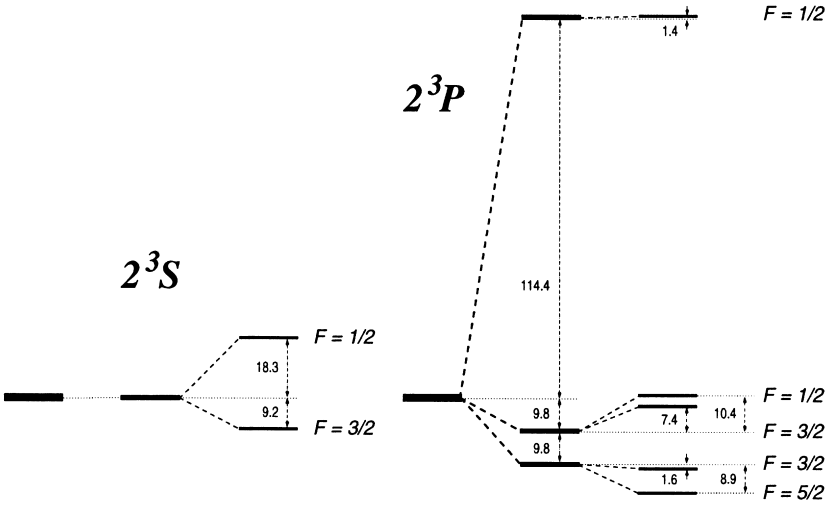

Fig. 3. The fine structure and hyperfine structure of the triplet states, 2^3S and 2^3P, relevant for the metastability exchange optical pumping of ^3He. The energy splitting of each level is given in μeV.

When an atom is positioned in an external magnetic field of intensity B_0 the hyperfine levels will split due to the interaction of the atom with this field. The result is that the $(2F + 1)$-fold degeneracy of each level will now be completely removed. At the field strength of ≈ 40 G of the present experiment Zeeman splitting of the hyperfine states is in the order of 0.01 μeV [18] and is negligible compared to the hyperfine structure splitting.

4.2. Metastability exchange optical pumping of ^3He

The concept of the optical pumping technique [21] is that through transfer of angular momentum from photons (polarized light) to the atomic electrons, large unequal populations of atomic magnetic substates can be created. The polarization of ^3He gas by optical pumping can be achieved with two techniques presently available, namely by the spin–spin interaction with an optically pumped Rb vapour [22] and by metastability exchange with optically pumped ^3He atoms in their $1s2s^3S_1$ state [23]. For the development of new targets in nuclear and particle physics experiments, both the spin exchange and the metastability exchange methods became feasible when high power laser systems were commercially available at the wavelengths of the resonance lines, $\lambda = 794.8$ nm and $\lambda = 1083$ nm [24], respectively.

Colegrove and Franken first reported the alignment of ^4He atoms in the metastable triplet 2^3S_1 state [25]. They showed that nuclear polarization could be obtained by optical pumping of ^3He. The polarized ^3He target described here is based on this principle [26–28]. The 2^3S_1–2^3P transitions are used in the polarization of the ^3He nucleus by metastability exchange optical pumping. The ^3He nuclei are polarized indirectly and the method is based on the existence of metastable ^3He atoms ($^3He^*$) in the 2^3S_1 state. When a weak RF discharge is ignited in a gas sample, at a typical pressure of approximately 1 mbar, the ratio of metastable to ground-state ^3He atoms is about 10^{-6}. Under these conditions the metastable state has a lifetime of about 10^{-3} s [29]. The transitions between the 2^3S_1 state and the 2^3P states are optically pumped by either right-handed (σ^+; $\Delta m_F = +1$) or left-handed circularly polarized light (σ^-; $\Delta m_F = -1$).

The scheme of polarizing ^3He nuclei is given in Fig. 4, which shows the relevant hyperfine levels involved in optical pumping of ^3He. When the ^3He gas sample is irradiated with light at $\lambda \approx 1083$ nm, nine transitions between the hyperfine levels of the

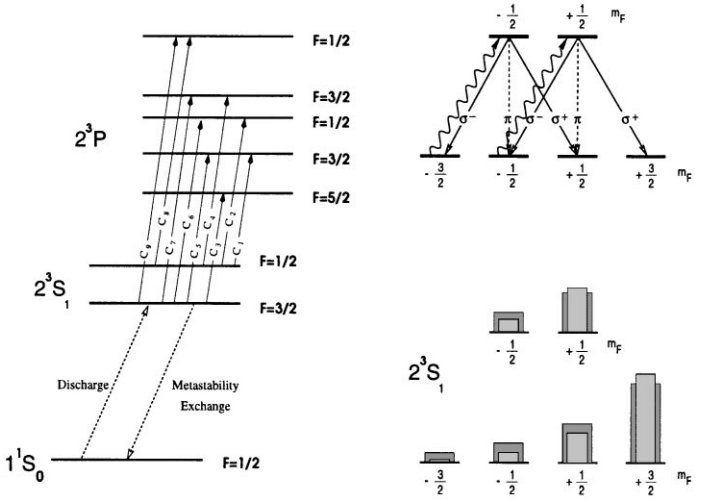

Fig. 4. A schematic overview of metastability exchange optical pumping of ^{3}He. The left diagram shows the nine optical transitions between the 2^3S and 2^3P states of ^{3}He. Top-right: The optical pumping scheme of metastable ^{3}He atoms with impinging right-handed (σ^+) circular polarized light for the C_9 transition. Bottom-right: The height of the light (dark) shaded columns indicate the distributions of the m_F levels for a nuclear polarization P = 0.50 (0.33).

2^3S_1 state and the 2^3P states (C_1, C_2, …, C_9) are possible. When σ^+ light is incident on the gas sample along a weak homogeneous magnetic field, of about 1 mT, only transitions are induced according to the selection rule $\Delta L = 1$ and $\Delta m_F = +1$. Calculations [30] predict that in our pressure regime the highest polarization is achieved by pumping via the C_8 or C_9 transitions. We have also experimentally confirmed this. The main reason is that due to Doppler broadening and small hyperfine splitting the transitions C_1–C_7 overlap and since these transitions involve different hyperfine levels, no significant level of polarization can be obtained.

Gas kinetic collisions in the ^{3}He ensemble (with a cross section $\sigma = 7.6 \times 10^{-16}$ cm^2 at 300 K [31]) lead to a relaxation of the orientation of the hyperfine levels of the 2^3P-triplet within the lifetime of $\tau_{2^3P} \approx 10^{-7}$ s [32]. The de-excitation of the atoms can be considered isotropic and is distributed over all nine transitions C_1 to C_9 of the $2^3P \rightarrow 2^3S_1$ multiplet. This *collisional mixing* is complete in our pressure regime, which means that all the magnetic sublevels of the 2^3P-triplet are equally populated within the lifetime of the excited state [33]. The fluorescence light of the isotropic decay to the metastable 2^3S_1 state is consequently unpolarized. Therefore, by repeated absorption and spontaneous emission cycles, in other words by depopulation pumping [21] of the lower m_F levels, the population distribution is shifted towards the higher m_F levels. Next, the polarization of the metastable atoms is transferred to the nuclear spin of the ground-state atoms via so-called *metastability exchange* collisions

$$^3\overrightarrow{He} + {}^3He \rightarrow {}^3\overrightarrow{He} + {}^3He^*. \quad (1)$$

Due to the short duration of these collisions ($\approx 10^{-12}$ s) compared to the time scale of the hyperfine interaction ($\approx 10^{-9}$ s), the electron and the nuclear spins are entirely uncorrelated, hence the nuclear spin is unaffected by these collisions [34]. In such collisions the metastable atom exchanges its excitation energy with the ground-state atom. This results after the collision in a ground-state atom with a polarized nucleus and an unpolarized metastable atom which can be polarized again within its sufficiently long lifetime of about 10^{-3} s through absorption of polarized laser light. Due to its high cross-section, metastability exchangeis the dominant reaction in the ^{3}He atomic ensemble, which implies that the polarization of

ground-state atoms equals the polarization of metastable atoms.

At an output power of 10 W, circularly polarized laser light represents a *pumping power* of about 10^{20} light quanta s^{-1} incident on a sample of N ^{3}He atoms. The efficiency with which angular momentum is transferred to the ^{3}He atoms is a function of the polarization P and vanishes when P approaches unity. The polarization P is given by

$$P = \frac{N_+ - N_-}{N_+ + N_-} = \frac{n(m_F + 1) - n(m_F)}{n(m_F + 1) + n(m_F)}. \quad (2)$$

Here, $N_+(N_-)$ represent the number of atoms with nuclear spin projection $m_I = +\frac{1}{2}(-\frac{1}{2})$ and $n(m_F)$ the occupation number of the hyperfine level with magnetic quantum number m_F. A calculation of the nuclear polarization in the pumping region as a function of the intensity of the irradiated laser light, the densities of ground-state and metastable atoms, the exchange channels of Eq. (1) and the relaxation time T_1, has been performed by Nacher and Leduc [35,36]. For the purpose of our target it is sufficient to describe the optical pumping scheme by assuming spin–temperature equilibrium, which is valid as long as the metastability exchange process is much faster than the average optical pumping cycle. The metastable atoms are then exponentially distributed over the m_F hyperfine levels according to $n(m_F) = N_0 e^{\beta m_F}$, with $\beta = \ln[n(m_F + 1)/n(m_F)]$. In the limit of spin–temperature equilibrium the optical pumping scheme reduces to a single rate equation [29] for the nuclear polarization P as a function of three basic experimental observables: the photon absorption rate of the unpolarized gas, $R_0 \equiv R(P = 0)$; the total number of ^{3}He atoms in the pumping region, N; and the longitudinal relaxation time under pumping conditions, T_1. The time dependence of the nuclear polarization can be determined for any of the optical pumping transitions between the 2^3S and 2^3P states. Relaxation terms due to lattice relaxation (T_1), imperfect circular polarization (ε) of the laser light and reabsorption of unpolarized fluorescence light (ρ) are included in the rate equation. The steady-state solution, $P_{eq}(dP/dt = 0)$ is now written as a function of a single pumping parameter $A = R_0 T_1/N$ [26]. Fig. 5 shows the evolution of P_{eq} as a function of A.

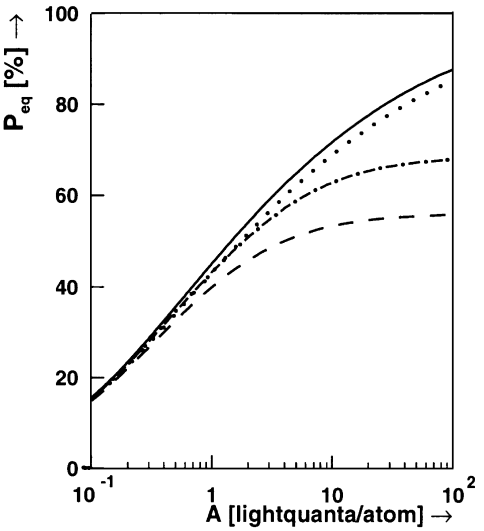

Fig. 5. Equilibrium polarization P_{eq} as a function of the pumping parameter $A \equiv R_0 T_1/N$, calculated for the C_9 transition (full curve). Depolarization effects due to reabsorption of unpolarized fluorescence light from the 2^3P state (ρ) and as a result of imperfect circular polarization of the incident laser light (ε) are also included, e.g. dotted curve: $\varepsilon = 0.00$ and $\rho = 0.20$; dot-dashed: $\varepsilon = 0.01$ and $\rho = 0.00$ curve; dashed curve: $\varepsilon = 0.03$ and $\rho = 0.00$.

Fig. 6 shows the result of a fit to the data, both to the rate equation from Ref. [26] (corresponding to the C_9 transition) and to a single exponential, i.e. $P(t) = P_{eq}(1 - e^{-t/\tau_p})$. The discrepancy between the exponential fit and the data indicates that the pumping rate decreases with increasing polarization, which is indeed consistent with the decrease in absorbed laser light by the ^{3}He gas.

4.3. Spin relaxation mechanisms

Several mechanisms exist that may limit the achievable polarization. For example, Fig. 5 shows the reduction of the polarization due to a small component of pumping light of opposite handedness as well as the effect of unpolarized fluorescence light within the gas sample. It apparently shows that reabsorption does not depolarize as strongly as the wrong handedness of the circular polarization of the pumping light, especially at high equilibrium polarization.

The mechanisms mentioned above are *light-induced* relaxation mechanisms and will not affect the

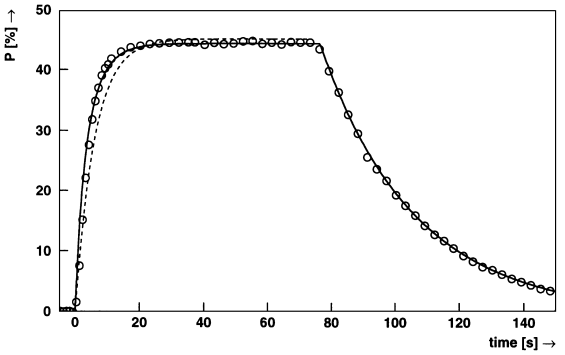

Fig. 6. Measured target polarization (closed circles) as a function of time. The solid curve represents the calculated ^{3}He polarization for the C_9 transition, with the corresponding optical pumping parameters $A = 1.73, \varepsilon = 0.03$ and $\rho = 0.04$. At $t = 74$ s the laser light is blocked and the nuclear relaxation is fitted to e^{-t/T_1}, with the longitudinal relaxation time $T_1 = 29.4$ s. The dashed curve is the result of the fit to the data with a single exponential.

polarization when the laser light is blocked. In the present set-up, spin relaxation is dominated by spin–lattice interactions, i.e. interactions of polarized ^{3}He atoms with their environment. These interactions contribute to the longitudinal relaxation time T_1. The relaxation time can be divided into four major contributions of different origin, which can be added up as follows:

$$\frac{1}{T_1} = \frac{1}{T_{\text{grad}}} + \frac{1}{T_{\text{latt}}} + \frac{1}{T_{\text{rf}}} + \frac{1}{T_{\text{res}}}. \quad (3)$$

The resulting relaxation time T_1 arises from the presence of magnetic field gradients (T_{grad}) [37,38], spin–lattice interactions (T_{latt}) [39–41], collisions with products in the discharge (T_{rf}) and from the finite residence time (T_{res}) of the ^{3}He atoms in the optical pumping region. Spin–lattice relaxation in our set-up is dominated by the presence of the discharge in the pumping region. In our system we used frequencies of 170 kHz and 20 MHz and we have observed that the higher frequency gave better results for polarization and pumping rates (see also Ref. [42]). However, maximum polarization is achieved when using the 20 MHz discharge in combination with a weak 170 kHz discharge.

5. Polarized ^{3}He target set-up

The polarized ^{3}He target (see Fig. 7) was developed in three phases. First the technique of metastability exchange optical pumping of ^{3}He atoms was applied to sealed cells. This allowed for optimization of the laser system, optical polarimeter and the system for rapid reversal of the target polarization. Next, measurements were carried out on a flowing system in order to study the achievable figure of merit, which is defined as $\text{FOM} = P_{\text{eq}}^2 f$, with P_{eq} the equilibrium target polarization at a gas flow f. Studies of relaxation mechanisms of the nuclear polarization were performed on both sealed cells and on the flowing system. The last phase was the development of the cryogenics for the storage cell. An important aspect of the target is the interface of the optical pumping region, where the ^{3}He nuclei are polarized, to the vacuum system of the AmPS storage ring. These are discussed in separate sections. Finally, a remote-control system was developed in order to control the target system from outside the IT hall of the AmPS facility.

5.1. Magnetic holding field

A polarized target requires a magnetic holding field, $\boldsymbol{B}_0$, to provide a quantization axis along which the atoms are polarized. The magnetic field intensity and the homogeneity, in the area of the pumping and storage cell, give the two main constraints for the design of the coils which produce the holding field. When we require that the depolarization effects due to field gradients are smaller than the relaxation due to surface effects, a relative field gradient of $\Delta B/B_0 \leq 10^{-4}\,\text{cm}^{-1}$ is required [37,38], with ΔB the magnetic field gradient per cm averaged over the pumping cell region. This can be realized by use of a Helmholtz coil configuration. To position the ^{3}He nuclear spin in any desired direction in space three sets of Helmholtz coils (HHC) were built, with average diameters of 104.2, 114.2 and 128.2 cm, as shown in Figs. 8 and 20. Relaxation measurements show that for a sealed pumping cell with similar dimensions as the pumping cell used in the experiment a longitudinal relaxation times of $\tau_{\text{grad}} > 1000$ s can be obtained. These measurements were performed

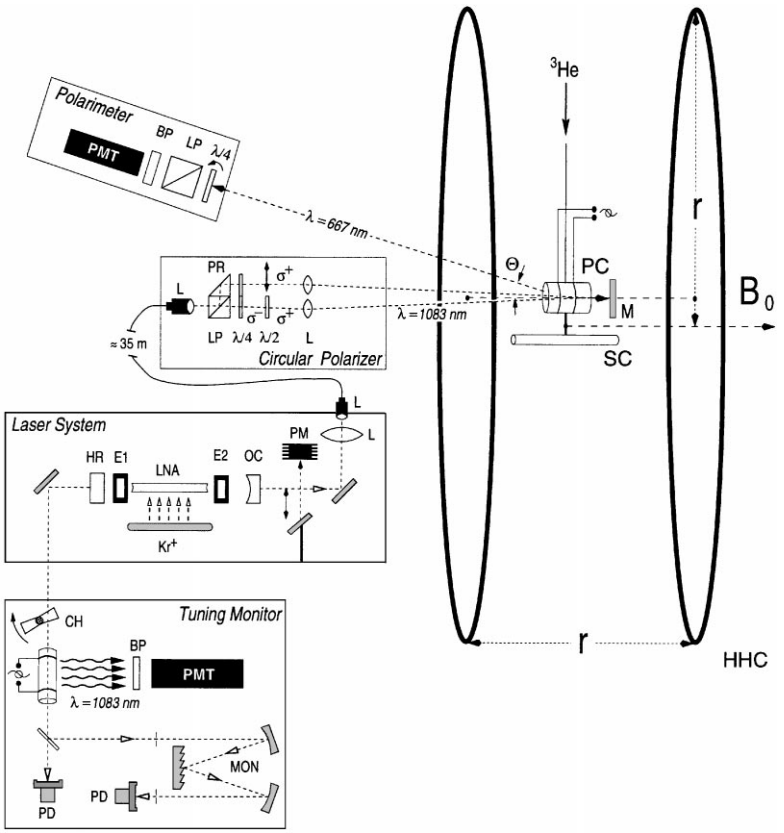

Fig. 7. A schematic layout of the optical pumping system of the polarized ^{3}He target, showing the LNA laser system, optical fiber, circular polarizer, tuning monitor, pumping cell (PC), storage cell (SC), Helmholtz coils (HHC) and optical polarimeter. The various optical components are described in the text.

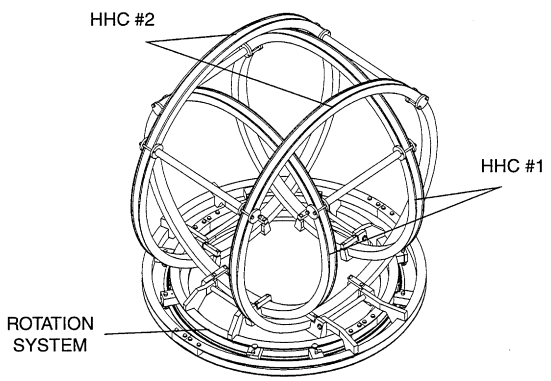

Fig. 8. Overview of the Helmholtz coils support- and rotation system, showing two sets of coils needed to position the holding field direction at any angle in the scattering plane. The set that defines the quantization axis normal to the scattering plane is not shown.

with the Helmholtz coil with the smallest diameter (the two larger sets of Helmholtz coils should give even better results for a pumping cell of the same geometry).

As the polarization decay is related to the relative field gradient in the holding field, various distortions of the Helmholtz field due to external fields can be compensated by increasing the magnitude B_0. Obviously, this does not work when a magnetizable object is causing a gradient in the pumping cell. Therefore, mainly aluminum or high-quality non-magnetic stainless steel (316 or A4 quality) was chosen as construction material for the target chamber and its support system.

Increasing the intensity of the holding field results in a larger deflection of the electron beam that traverses the target chamber. This deflection can be

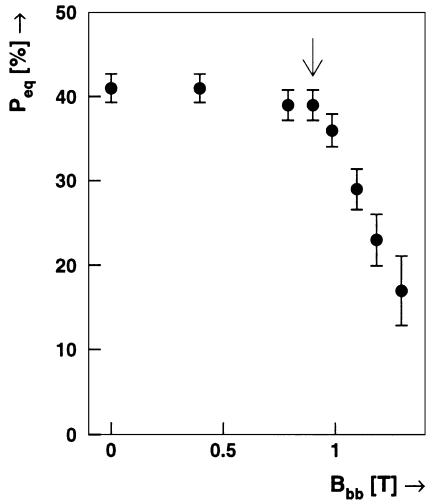

Fig. 9. Target polarization as a function of the magnetic field strength of the Bigbite spectrometer. The arrow indicates the value at which the spectrometer is operated ($B_{bb} = 0.9$ T) during the electron scattering experiment.

corrected with steering coils placed at both ends of the target chamber. The Bigbite spectrometer with its 1 T magnetic field was the main source of field gradients at the position of the target. To reduce these gradients, a field clamp was connected to the iron yoke of the spectrometer. Due to saturation effects the fringe fields of the electron spectrometer became significant (i.e. causing gradients > 30 mG cm^{-1} near the target) when the magnetic field strength increased above 1 T. Fig. 9 shows that the relaxation of the nuclear polarization rapidly increases when the Bigbite field (B_{bb}) is set above the nominal value of 0.9 T.

5.2. Laser system

An intense continuous source of radiation at a wavelength of 1083 nm and with a narrow bandwidth is required to optically pump the ^{3}He metastables to an acceptable polarization at the required atomic flow [43]. The best results are currently obtained with a crystal that uses the $^4F_{3/2} \rightarrow {}^4I_{11/2}$ transition of the Nd^{3+} ions. Its chemical composition is given by $La_{1-x}Nd_xMgAl_{11}O_{19}$ ($x = 0.15$) and is usually described as Nd:LMA or LNA [44]. In the beginning of this decade the performance of LNA was superior compared to the earlier techniques with ^{4}He flash lamps and Nd:YAP lasers, i.e. high power (> 5 W), a well-matched bandwidth to the Doppler-broadened optical transition of the ^{3}He gas, and primary emission peaks close to the optical pumping transition [45].

For the polarized ^{3}He target of this experiment, a Laser Applications Model 9560 YAG laser system was used, where the Nd : YAG crystal was replaced by a LNA crystal manufactured by Union Carbide in Washougal, WA, USA. The cylindrical shaped laser crystal (4 mm in diameter and 79 mm long) was cut along the *a* axis of the crystal lattice [46]. The optical pumping set-up is schematically shown in Fig. 7. The LNA crystal is pumped by a Kr^+ arc lamp, type NL4491 from Heraeus-Noblelight (Cambridge, England), typically driven with a power of a few kW. Both were continuously cooled by flowing demineralized water through the cavity block. The water temperature was kept at 23°C and was stabilized within one degree. Temperature gradients between the centre and the surface of the crystal cause thermal lensing in the laser crystal, which may cause a focus of the laser light inside the cavity which can result in breaking of the laser crystal. This severely limits the pumping power of the Kr^+ arc lamp and its current was therefore restricted to about 21 A. The crystal ends were polished concave with a radius of 60 cm on both sides, in order to counteract the effect of thermal lensing of the LNA crystal. To minimize loss of power at the ends an anti-reflective coating was applied.

The laser cavity was built according to the scheme of Aminoff et al. [24], which has been adopted by most users of LNA lasers [26,27,42]. The laser cavity contains two uncoated etalons, of 0.3 and 1.0 mm thickness, to tune the frequency from the primary peak of the fluorescence spectrum to one of the optical pumping transitions. This results in a bandwidth of about 2 GHz, which is close to the Doppler width of the ^{3}He atoms. With this scheme it is possible to resolve the desired C_8 or C_9 transition. Tuning of the laser was facilitated by passing the light that exits the high reflectivity cavity mirror through a sealed ^{3}He discharge cell and by observing the fluorescence signal in

a PMT (Hamamatsu R-316-02), positioned transverse to the laser path. Tuning of the laser at the required wavelength is in fact changing the optical path length of the light inside the laser cavity. By positioning an etalon inside the cavity the bandwidth of the natural fluorescence light of LNA is reduced by multiple beam interference inside the etalon. This can be done by either tilting the etalon with respect to the beam to change the path length, or by heating the etalon to change the index of refraction. Fig. 10 shows the ^{3}He polarization and the fluorescence signal V_{tune} of the laser system versus the temperature of both etalons. A system designed at NIKHEF was used to tune the etalon temperature and angle (see E1 and E2 in Fig. 7). The temperature of the etalon was measured by Pt100 temperature sensors and regulated by a 30 W resistive heater, connected to a Shimaden-SR25 PID controller. Some dedicated electronics was added to stabilize the temperature of the etalon within 0.1°C. Oriel DC encoder mike controllers (type 18222) were used to remotely control the angle of the etalons.

The best off-line results were obtained on a sealed cell with a diameter of 47 mm and length of 170 mm and a ^{3}He pressure of 0.56 mbar, shown in Fig. 11. The laser cavity consisted of two plano-concave mirrors as shown in Fig. 7. An output coupler (OC) with a reflectivity $R = 99.0\%$ and radius $r = 350$ mm and a high reflectivity rear mirror (HR), $R \approx 100\%$ and $r = 500$ mm, at 25.0 and 14.2 cm from the centre of the LNA crystal were used, respectively. Both mirrors as well as the etalons were acquired from Virgo Optics. The maximum output power of the laser in *free running* mode was $P_L \approx 11$ W at a lamp current of 19 A. The etalons are set under a small angle (< 5 mrad) to suppress undesired modes in the cavity which can occur when the etalons are kept transverse to the beam path and are only tuned through

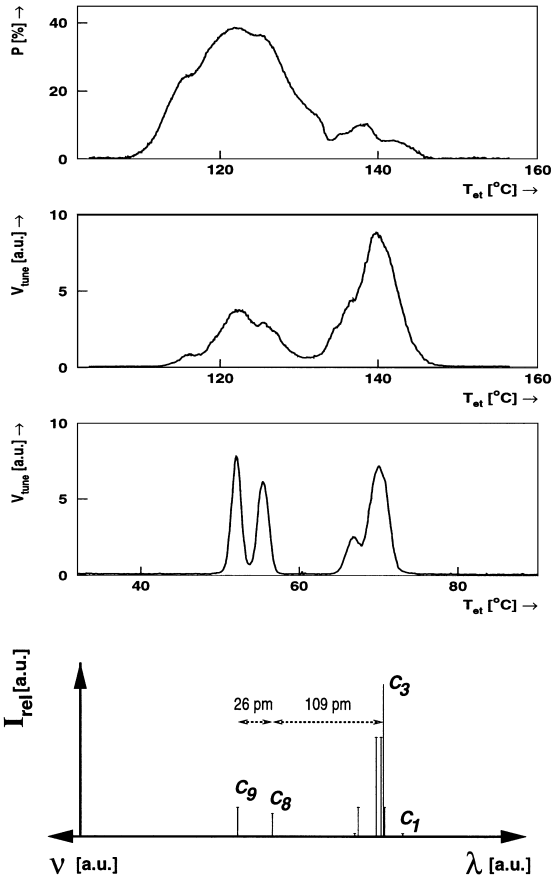

Fig. 10. Polarization dependence on laser tuning. The top two graphs show the ^{3}He polarization and the fluorescence signal V_{tune} of the laser tuning monitor versus the temperature of the 0.3 mm thick etalon. The third graph shows the tuning signal versus the temperature of the 1.0 mm thick etalon, while the temperature of the 0.3 mm thick etalon is set at about 130°C. The bottom picture shows a schematic overview of the relative intensities and the wavelength separation of all nine (C_1–C_9) $2^3S \rightarrow 2^3P$ transitions.

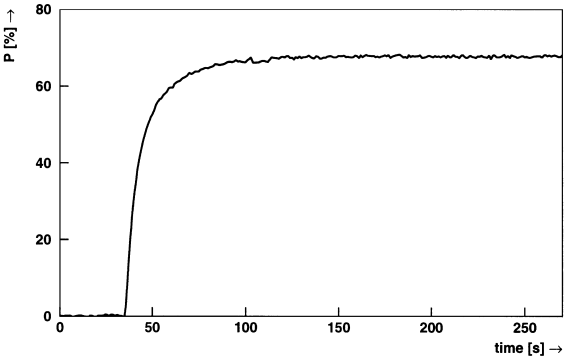

Fig. 11. Nuclear polarization for ^{3}He versus time measured on a sealed cell ($V \approx 400$ ml and $p = 0.56$ mbar). At an equilibrium polarization of 0.68 the achieved pumping rate is about 3.3×10^{17} at s^{-1}.

changing their temperature. This leads to an output of $P_L \approx 8.9$ W with just the 0.3 mm thick etalon and $P_L \approx 5.1$ W when in addition the 1.0 mm thick etalon is inserted.

A significant improvement in the laser system was achieved by using a different configuration in which the laser cavity consisted of a plano-concave ($r = 600$ mm) output coupler ($R = 99.2\%$) and a plano-plano high-reflectivity mirror ($R \approx 100\%$), respectively positioned at 345 and 300 mm away from the center of the LNA crystal. This resulted at a lamp current of 21.8 A in a laser power of 13 W in free running mode, 10.5 W with only the 0.3 mm thick etalon and 9.3 W with both the 0.3 and 1.0 mm thick etalons inserted in the laser cavity.

The complete laser system was positioned inside a light-tight and temperature stabilized room with air filters, placed outside of the electron scattering area. This allowed access to the laser system without interrupting the experiment, and reduced the frequency with which the laser optics needed to be cleaned to maintain adequate laser power. The infrared laser radiation was transported to the optical pumping cell with an optical fiber (type 0.39NA/FT-1.0-EMT) obtained from Thorlabs Inc. (Newton, USA), see Fig. 7. The laser light was coupled into the optical fibre via a set of two lenses, where the second lens was placed inside a high accuracy positioning stage to achieve optimal transmission of the laser light. The light exiting the optical fibre was coupled into a *circular polarizer* box (see Fig. 12) containing the optics to make a collimated beamspot of circularly polarized light on the optical pumping cell.

Fig. 13 shows the polarization and the pumping rate as a function of the effective laser power P_L^{eff}, with $P_L^{\text{eff}} \equiv 2\eta_T P_L$. Here, η_T is equal to the transmission efficiency of the optical fibre system and the factor two is due to the mirror behind ($R \approx 100\%$) the pumping cell. The curve is the result for the equilibrium polarization that can be obtained, as a function of the pumping rate calculated for the C_9 transition according to the model in Ref. [26]. The discrepancy between the data and the curve can be explained due to temperature instabilities, resulting in tuning shifts, when the data were taken.

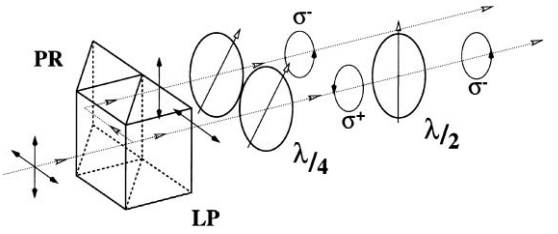

Fig. 12. Schematic overview of the polarizing optics used to produce circular polarized light. The linear polarizer cube (LP), prism (PR), two quarter-wave plates ($\lambda/4$) and a half-wave plate ($\lambda/2$) are shown. The arrows indicate the *fast* optical axis. The $\lambda/2$ plate is positioned at an angle $\pi/4$ with respect to the $\lambda/4$ plates.

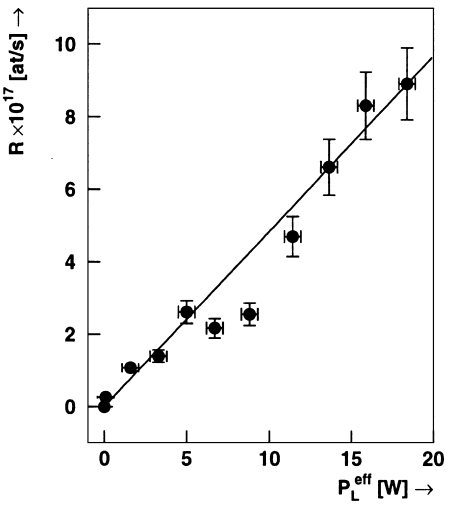

Fig. 13. Achieved pumping rates ($R \equiv P_{eq} N/\tau_p$) as a function of the effective laser power P_L^{eff} (tuned at C_9) incident on the ^{3}He gas sample, measured at a constant ^{3}He flow (1×10^{17} at s) and discharge intensity. The curve is the result for the equilibrium polarization as a function of the pumping rate calculated for the C_9 transition.

5.3. Pumping cell and gas feed system

The construction of the pumping cell is constrained by the gas pressure required inside the pumping cell and atomic flux into the target storage cell. Highest polarization is obtained for a pumping cell pressure of 0.5–1.0 mbar [42]. A schematic diagram of the gas feed system connected to the pumping cell is given in Fig. 14. The system allows for maintaining a constant inlet pressure p_0, resulting in a stationary flow f through the conductance C_1 ($\approx 10^{-3}$ l s^{-1}), into the optical

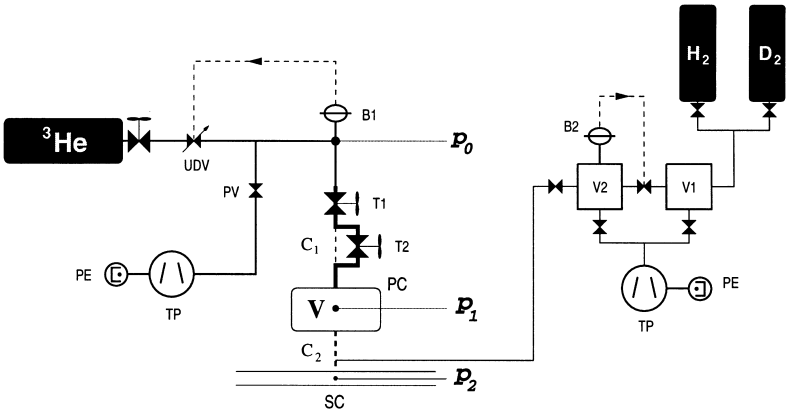

Fig. 14. Schematic layout of the polarized ^{3}He target gasfeed system and the H_2 and D_2 buffer system. The cylindrical (glass) pumping cell (PC) with volume V provided with two teflon hand-valves (T1 and T2), and the cylindrical storage cell (SC) are shown. The inlet pressure (p_0), measured with a baratron (B1), is regulated by a thermal regulating valve (UDV). The ^{3}He gas flow is determined by two capillaries (C_1 and C_2). See text for a more detailed description.

pumping cell. The inlet capillary C_1 can be bypassed by opening the second teflon valve T2. The pressure p_1 inside the volume V (508 ml) of the Pyrex pumping cell [27] is kept constant. Because $p_2 \ll p_1$, the flow f is determined by the pressure p_1 and the exit conductance C_2 of the pumping cell.

The ^{3}He gas used had a chemical purity of 99.995% and an isotopic enrichment of 99.9999%. It was purchased in 1.4 l bottles filled with 3 bar l from Isotec Inc. (USA). In order to establish an equilibrium flow the pressure p_0, measured with an MKS 122AA capacitive baratron gauge (B1), was used as a feedback for the Balzers UDV135 thermovalve (UDV). Due to the depolarizing effects of the metal surface a baratron gauge could not permanently be connected to the pumping cell and therefore a cross calibration of the inlet pressure p_0 versus the pumping cell pressure p_1 for various stationary flows was performed prior to the experiment. For calibration and tuning of the detector set-up a separate H_2 and D_2 buffer system was used. The inlet pressure of these gases was regulated by maintaining a constant pressure of about 1–10 mbar, measured by an MKS640A baratron (B2), in a known volume $V2$ and letting the gas bleed out through a copper capillary of about 2.5 m length (1.0 mm diameter) into a specially designed interface between the storage cell and the end of the glass exit capillary (C_2) of the pumping cell.

The equilibrium ^{3}He flow f is ($p_1 \gg p_2$) is given by

$$f = C_1(p_0 - p_1) = C_2 p_1 \Leftrightarrow \frac{p_1}{p_0} = \frac{C_1}{C_2 + C_1}. \quad (4)$$

The pumping cell pressure is typically in the order of a few mbar, and as a consequence the gas flow through conductances C_1 and C_2 is in the intermediate flow regime [47]. Hence, C_1 and C_2 are a function of the pressures p_0 and p_1. Thus, either C_1 or C_2 has to be known as a function of the pressure p_0 (or p_1) to determine the absolute value of the flow through the pumping cell. The conductances C_1 and C_2 consist of precision capillaries with inner diameter of 0.5 and 1.0 mm and length of 50.0 and 60.0 mm, respectively. The flux f is related to the time derivative of the pumping cell pressure p_1 by $f = V(k_B T)^{-1}\, dp_1/dt$, where k_B is the Boltzmann constant and T the pumping cell temperature. When the pressure decay p_1 is measured as a function of time after closing the first teflon valve (T1), a dp_1/dt curve can be constructed versus the pumping cell pressure p_1. By accurately determining the volume of the pumping cell between the first teflon valve and the beginning of the exit conductance C_2, the flow can be directly be determined from the pumping cell pressure. Because the pumping cell pressure is not measured while the polarized target is operational the

resulting flux f is calculated from the inlet pressure. The average residence time T_{res}, to calculate the longitudinal relaxation time T_1 (see Eq. (3)), of a ^{3}He atom inside a volume V is given by

$$T_{res} = p_1 V/f = V/C_2. \quad (5)$$

At a constant laser power the achievable ^{3}He polarization will decrease when the gas flow is increased. The maximum polarization will be obtained at a zero flow, i.e. when the ^{3}He gas is contained in a sealed pumping cell. Fig. 15 shows the target polarization and the figure of merit as a function of the ^{3}He gas flow. It shows that the FOM increases about 50% when the gas flow is changed from 1×10^{17} to 2.5×10^{17} at s^{-1}. For the electron scattering experiments the flow was set at 1×10^{17} at s^{-1} as a result of an optimization that also took into account the lifetime of the stored electron beam and the count rates of the detector set-up.

5.4. Cryogenic storage cell

A storage cell is used to increase the integrated target thickness without affecting the quality of the circulating beam. It consists of a cylindrical tube through which the electron beam is directed. In the centre of the storage cell an entrance tube is connected to facilitate the injection of the (polarized) target gas. The conductance of a tube (length $L/2$ and diameter D, both in cm), for a gas with molecular mass M (in amu) at a temperature T (in K), is in the regime of molecular flow given by [47]

$$C \approx 3.8\sqrt{\frac{T}{M}}\left(\frac{D^3}{L/2}\right). \quad (6)$$

When the target gas is fed into the centre of the storage cell at a flow f, there will be a density distribution $\rho(z)$ of approximately triangular shape inside the tube of the storage cell. This distribution has a maximum at the cell centre of $\rho(0) = f/C_{cell}$, with $C_{cell} = 2C$. The resulting integrated target thickness is given by $t = \rho(0)L/2$. The luminosity $\mathscr{L}$ can be written as ($L \gg D$)

$$\mathscr{L} \approx I_e f \frac{(L/2)^2}{7.6D^3}\sqrt{\frac{M}{T}} \text{ (e at cm}^{-2}\text{ s}^{-1}\text{)}. \quad (7)$$

The above expression shows that an increased target density can be obtained by (i) increasing the length, (ii) decreasing the aperture and (iii) decreasing the temperature of the storage cell. The limits of these storage cell parameters are given by the intrinsic properties of the circulating electron beam and its interaction with the cell-wall material. The minimum diameter of the storage cell is dictated by

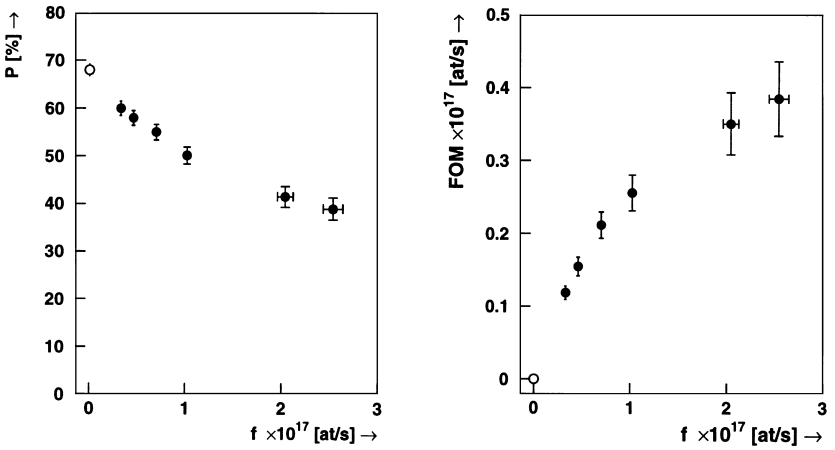

Fig. 15. Target polarization (left) and figure of merit, FOM $\equiv P^2 f$, (right) versus the ^{3}He gas flow f. The open circle is the result achieved on a sealed cell.

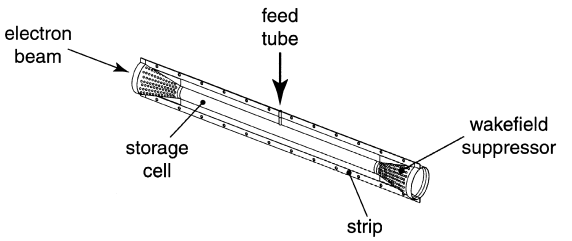

Fig. 16. View of the aluminum storage cell ($L = 400$ mm, $D = 15$ mm and $t = 60$ μm). Not shown is the mylar window ($l = 360$ mm, $h = 6$ mm and $t = 0.9$ μm), which is integrated in one side of the storage cell.

the spatial charge distribution in the transverse direction of the stored beam. Processes, such as interaction with both the target gas and the residual gas will result in broadening of this distribution. Beam-lifetime studies [48] show that the transverse charge distribution of the beam has a long non-gaussian tail. For our experiments the optimal dimensions of the storage cell are a diameter of 15 mm and a length of 400 mm. Ultra-pure aluminum (99.95%) was selected as cell material. This material is non-magnetic and has an excellent thermal conductivity at cryogenic temperatures ($\lambda \simeq 40$ W cm^{-1} K^{-1} at 15 K).

Fig. 16 shows the storage cell of the present experiment. The cell is constructed from an aluminium foil of thickness $t = 60$ μm and features a 300×4 mm^2 window of 0.9 μm thick mylar placed in the wall of the target cell which faces the silicon-strip detector. The storage cell is placed inside a U-shaped frame, which facilitates easy exchange of storage cells, for example with different diameters. This frame mounts in a heat-shield with titanium springs ($L = 40$ mm; $A = 0.05 \times 20$ mm^2), thereby taking advantage of the poor thermal conductance of titanium ($\lambda \approx 0.035$ W mm^{-1} K^{-1}). The heat shield is connected to the room temperature structure with a similar connection. These springs are shaped such that the thermal distortion of the storage cell transverse to the electron beam is minimized when it is cooled down. In order to minimize movement parallel to the beam two titanium rods ($L = 38$ and 30 mm; $D = 7.1$ mm^2) connect the cell frame to the heat shield and the heat shield to the structure at room temperature.

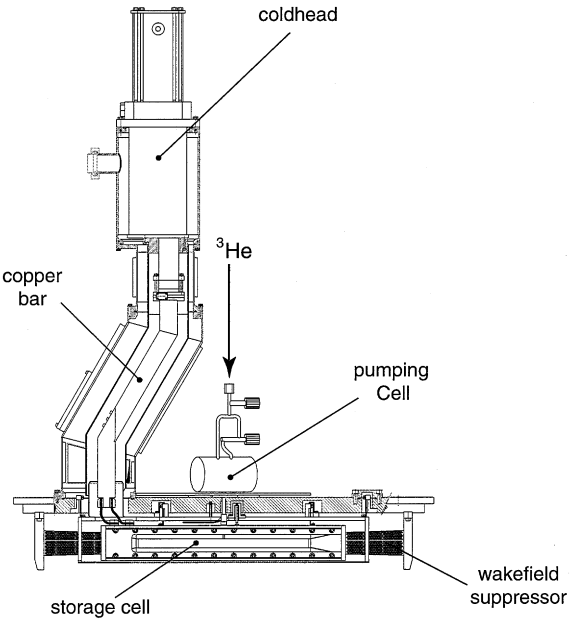

Fig. 17. Overview of the cryogenic target setup. Heat is transferred from the storage cell to a two-stage coldhead with four flexible copper braids and an ultra-pure copper bar. Also shown are the glass pumping cell with two isolation teflon handvalves and wake field suppressors at both ends of the storage cell.

5.4.1. Cryogenic system

The storage cell frame was connected to a two-stage cryo-refrigerator, model CryoMech *GB37* (30 W maximum cooling power) from Cryomech Inc. in Syracuse (USA), see Fig. 17. It delivers 23 W of cooling power at 15 K at the second stage, when there is a 20 W heat load on the first stage [49]. The coldhead contains ferromagnetic components and it is therefore needed to position it away from the optical pumping cell. This is necessary because of spin relaxation of the polarized ^{3}He atoms due to the presence of magnetic field gradients, as discussed in Section 4.3. The coldhead is therefore positioned outside of the HHC configuration and is extended towards the storage cell with a copper bar (520 mm long, cross-sectional area 40×40 mm^2 and a conductivity $\lambda \simeq 15$ W cm^{-1} K^{-1} at 15 K) which is connected to the second stage of the coldhead. The aluminum mounting-frame of the storage cell is connected to the copper bar via a flexible copper braid. The bar and the flexible copper braid are covered with 10 to 15 layers of aluminized

mylar, in order to minimize the radiative heat load. The whole structure is surrounded by an aluminum heat shield, which is connected to the first stage of the coldhead and which is also covered with about 15 layers of aluminized mylar.

Electrons travelling through the AmPS storage ring induce a corresponding image charge in the beam pipe following the electrons around the ring. When an electron bunch passes a discontinuity in the beam pipe, the image charge generates wake fields in that section. These wake fields can cause energy loss in the beam (up to kW in our case) which translates into heating of components in the vicinity of the discontinuity of the beam pipe. In order to minimize power losses in the storage cell, two-stage wakefield suppressors were designed. The first stage consists of aluminum conical shaped tapers spotwelded to the target cell cylinder (see Fig. 16). The second stage of the wakefield suppressors are also conical shaped and need to be electrically connected to the storage cell, but thermally isolated. Hence, they are made from 145 mm long Cu–Be foils ($\lambda = 55\,\mathrm{mW\,mm^{-1}\,K^{-1}}$) with a cross-sectional area of $\approx 3.3\,\mathrm{mm^2}$, perforated with holes (total area $\approx 100\,\mathrm{cm^2}$) to increase the vacuum pumping speed and to reduce the amount of material.

A number of tests have been performed before the start of the experiment to optimize the cryogenic system and to establish the desired operating temperature. The minimum operating temperature is set by the spin-relaxation of polarized ^{3}He atoms on the cell walls (see Section 4.3). The temperature of the target system is monitored with five resistivity sensors, four carbon-glass sensors (CGR series) and one cernox sensor (CX series), obtained from Lake Shore Cryotronics Inc. (Ohio, USA). Only one sensor is mounted on the heat-shield of the target, the others are all connected to the second cooling stage of the cryogenic system. Cooling down of the storage cell typically took up to eight hours. Heating the target, in order to change the pumping cell and/or the storage cell, was facilitated with four 50 W heaters and usually could be accomplished in less than ten hours. These cycles of cooling down and heating up the target did not affect the shape and minimum temperature of the storage cell. The target temperature during the experiment was 17 K. Fig. 18 shows the count rates for the elastic scattering reaction $^3\overrightarrow{\mathrm{He}}$ $(\vec{e}, e'\,^3\mathrm{He})$ as a function of the target temperature, which is normalized to unity at 300 K. The curve is a fit of the $T^{-1/2}$ behaviour (see Eq. (7)) of the storage cell conductance, and is consistent with the data.

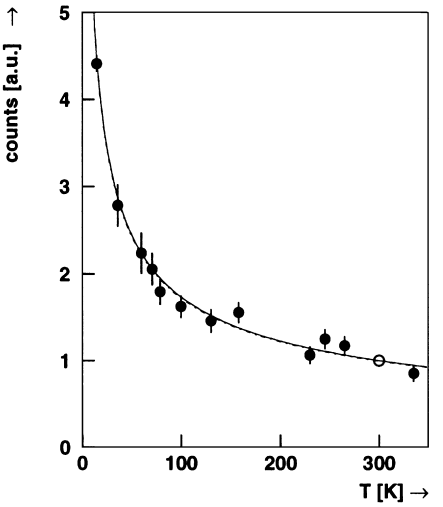

Fig. 18. Count rates for elastic electron scattering from ^{3}He versus the target temperature normalized to one at 300 K (open circle). The curve is a fit of the $T^{-1/2}$ behaviour of the storage cell conductance, which is consistent with the measured target temperature of 17 K.

5.5. Target vacuum chamber

For experiments in a storage ring such as AmPS, the base pressure typically ranges between 10^{-9} and 10^{-11} mbar. Since large gas throughputs are flown into the ring vacuum a powerful differential pumping system is required around the target, in order to maintain an adequate vacuum in the ring. A vacuum system was designed and constructed [50] to accommodate a ^{3}He gas flow of up to 1×10^{18} at $\mathrm{s^{-1}}$.

Fig. 19 shows the IT vacuum system, which consists of a high capacity, three-stage differential pumping system and a scattering chamber. The target chamber is pumped by two turbo-molecular pumps (Pfeiffer-Balzers TPU-2200; $3200\,\mathrm{l\,s^{-1}}$ for helium). The second and third chamber of the

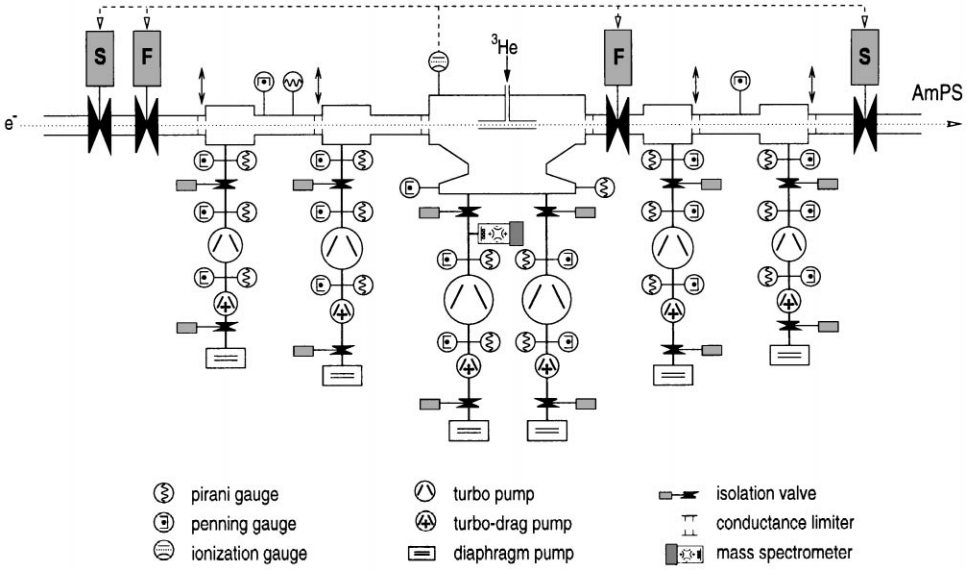

Fig. 19. Schematic layout of the internal target vacuum system. It consists of a three-stage differential pumping system with an overall pumping speed for ^{4}He of about $10^4\,l\,s^{-1}$. The entire internal target region can be isolated from the rest of the storage ring by a set of four valves. The dashed line indicates that these fast (F) and slow (S) valves are triggered by an ionization gauge, which is connected to the target chamber.

differential pumping set-up are also pumped by turbo-molecular pumps, but with reduced pumping speeds, respectively $1450\,l\,s^{-1}$ (Pfeiffer-Balzers TPU-1600) and $300\,l\,s^{-1}$ (Pfeiffer-Balzers TPU-510) for helium. To minimize the target gas flow into the storage ring, three pairs of conductance limiters are placed between the internal target vacuum chamber and the AmPS ring; the outer two pairs are movable, the inner pair is fixed. The conductance limiters consist of two kapton foils 56 mm apart with increasing diameter from the target chamber outwards. With a storage cell diameter of 15 mm these are respectively 20, 25 and 30 mm.

Fig. 20 shows the IT set-up for the present experiment. The TPU-2200 pumps are connected to the target chamber with a specially designed aluminium pump-out. The distance between the turbo-molecular pumps and the optical pumping cell is sufficiently large to eliminate relaxation effects due to field gradients (see Section 4.3), produced by ferromagnetic parts inside these pumps. At the same time it allows complete freedom for the Helmholtz coils to be positioned at any required angle. The scattering chamber has three removable side flanges and was constructed from aluminum, type ANP8000 (hardness = 140 brinell; maximum elasticity = 500 N mm^{-2}) in order to withstand the external forces when the target chamber is on vacuum. The top accommodates the flange for the storage cell, with its cooling and gas feed connections. The sides can both be covered with a 55 μm thick stainless steel (annealed AISI-309) exit foil, but in the present experiment this was done only at the side facing the Bigbite spectrometer. At the other side the silicon-strip detector was mounted on the scattering chamber via a special flange at a central angle of 70°.

5.6. Target polarimeter

To minimize the uncertainty in experimental asymmetries accurate and continuous measurement of the target polarization is imperative. A possible way of measuring nuclear polarization is through nuclear magnetic resonance (NMR). Unfortunately, NMR is not a convenient method for application in an accelerator environment. We have used a relatively simple optical technique for

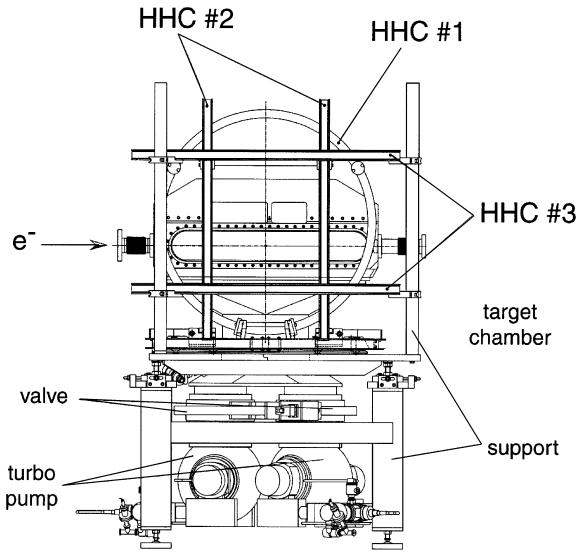

Fig. 20. Overview of the target scattering chamber and the support system. Shown are the aluminum vacuum chamber and pump-out, exit windows, two Pfeiffer-Balzers turbo molecular pumps with isolation valves and three sets of Helmholtz coils to orientate the target spin in every desired direction.

measuring the polarization inside the pumping cell, developed by Pavlović and Laloë [51,52]. The target polarimeter measures the degree of circular polarization in the $3^1D_2 \rightarrow 2^1P_1$ transition ($\lambda = 667$ nm), emitted in the discharge of the ^{3}He gas. This method relies on the conservation of nuclear polarization during collisions that excite atoms from the ground state to a higher state. In the excited state the hyperfine interaction partially transforms nuclear orientation to electronic orientation. Light emitted, when the atom decays through spontaneous emission, will show a degree of circular polarization $\mathscr{P}(\sigma^+, \sigma^-)$ proportional to the electronic polarization, hence reflecting the state of nuclear polarization. Two independent calibration measurements have been performed for this technique and resulted in a relation between the pumping cell pressure p_c and the ratio f_p of the ^{3}He nuclear polarization P_N and $\mathscr{P}(\sigma^+, \sigma^-)$, with a systematical uncertainty better than 2% [53,54].

The polarimeter (see Fig. 7) consists of a rotating quarter-wave ($\lambda/4$) plate ($\omega \approx 2\pi \times 80$ Hz), a linear polarizer cube (LP), an interference bandpass filter (BP, $\Delta\lambda_{\mathrm{FWHM}} = 10$ nm) and a photomultiplier tube (Philips XP2023B), all selected for a wavelength of 667 nm. The intensity of circular polarized light is modulated behind the linear polarizer cube that is positioned between the PMT and the rotating quarter-wave plate. A bandpass filter is used to suppress the light of the other ^{3}He transitions produced in the discharge. With this scheme the PMT produces an oscillating signal with an angular frequency of 2ω and an amplitude V_{AC} around a constant signal V_{DC}, given by

$$V_{\mathrm{PMT}} = V_{\mathrm{AC}} \sin 2\omega t + V_{\mathrm{DC}}. \tag{8}$$

The PMT signal is fed into an active filter, which splits the signal into a low-frequency (< 5 Hz) DC signal and a 'high' frequency ($5\ \mathrm{Hz} < \nu < 750$ Hz) AC signal. This module can amplify the DC signal with a factor 50, 100, 500 or 1000 after which it can be put directly into the data-acquisition system. The amplitude of the AC signal can be accurately determined with a lock-in amplifier (EG&G-5210), where the reference frequency is given by a LED-chopper coupled to the rotating $\lambda/4$-plate. Due to interference of the polarimeter with the laser light the polarization cannot be measured exactly on axis parallel to the holding field. Therefore, the polarimeter views the discharge in the pumping cell under a small angle θ (see Fig. 7). Off-axis the transmitted light will not only show $\sigma^{\pm}$ radiation, but it will also contain linearly polarized (π) light due to $\Delta m = 0$ transitions. It can be shown [54] that the angular dependence of the circularly polarized light is given by a $\cos\theta$ dependence, which is included in Eq. (9). The correction factor $v(B)$ is given by the field dependence of the hyperfine coupling between the nucleus and the electron cloud. The coupling decreases with increasing magnetic field strength and vanishes at high magnetic fields. This implies that the degree of circular polarization of the 667 nm line is also field dependent [54]. The resulting ratio of the two signals V_{AC} and V_{DC} gives the degree of circular polarization of the 667 nm line. The target polarization P is now given by

$$P = f_p \frac{v(B_0)}{\cos\theta} \frac{V_{\mathrm{AC}}}{V_{\mathrm{DC}}}. \tag{9}$$

where the pressure-dependent correction factor f_p is given by the result of Ref. [53,54]. The polarimeter

was systematically checked by placing a circular polarizer, consisting of a linear polarizer and a high-quality $\lambda/4$-plate, in front of the aperture. This yielded a signal as given by Eq. (8) with the ratio of V_{AC} over V_{DC} equal to unity. Small corrections to the deduced nuclear polarization can be made as described in Ref. [54].

6. Summary

A polarized ^{3}He internal target was developed and successfully employed for spin-dependent scattering experiments in the AmPS medium-energy electron storage ring at NIKHEF, Amsterdam. Target polarizations of 0.50 (0.42) at a flow of 1.0 $(2.0)\times10^{17}$ ^{3}He s^{-1} were obtained. Operation at a nominal flow of 1×10^{17} at s^{-1} resulted in a target thickness of 0.7×10^{15} at cm^{-2} at a target temperature of 17 K. The ^{3}He target was used in various scattering experiments with polarized electrons in the storage ring stacked to currents in excess of 110 mA. The flexibility in changing the orientation of the nuclear spin, in every required direction in space, was demonstrated in these experiments. The combination of a polarized internal target and a large acceptance detector set-up allowed successful data taking for the reaction $^3\overrightarrow{\text{He}}(\vec{e}, e'X)$ in several channels simultaneously, i.e. $X = 0$, p, n, pd^3, He ($X = 0$ stands for the inclusive channel) together with various kinematical settings.

References

[1] T.W. Donnelly, A.S. Raskin, Ann. Phys. 169 (1986) 247.
[2] B. Blankleider, R.M. Woloshyn, Phys. Rev. C 29 (1984) 538.
[3] J.F.J. van den Brand et al., Nucl. Instr. and Meth. A 402 (1998) 268.
[4] K. Ackerstaff et al., Phys. Lett. B 404 (1997) 383.
[5] H. Gao et al., Phys. Rev. C 50 (1994) R546.
[6] M. Meyerhoff et al., Phys. Lett. B 327 (1994) 201.
[7] K. Abe et al., Phys. Rev. Lett. 75 (1995) 25.
[8] P.L. Anthony et al., Phys. Rev. D 54 (1996) 6620.
[9] H.R. Poolman, Ph.D. Thesis, Vrije Universiteit, Amsterdam, Netherlands, 1999.
[10] J.F.J. van den Brand (spokesman) et al., NIKHEF Electron Scattering Proposal 94-05, 1994.
[11] B.W. Montague, Phys. Rep. 113 (1) (1984) 1.
[12] I. Passchier et al., Nucl. Instr. and Meth. A 414 (1998) 446.
[13] D.J.J. de Lange et al., Nucl. Instr. and Meth. A 406 (1998) 182.
[14] van den Brink et al., Nucl. Instr. and Meth. A 587 (1993) 657.
[15] M. van Sambeek, Thesis at the Vrije Universiteit Amsterdam, The Netherlands, 1997.
[16] D.W. Higinbotham et al., Nucl. Instr. and Meth. A 414 (1998) 332.
[17] H. Haken, H.C. Wolf, Atomic and Quantum Physics, 2nd edn., Springer Verlag, ISBN 3-540-17702-7 #2.
[18] Fred et al., Phys. Rev. 82 (3) (1951) 406.
[19] J.D. Prestage, C.E. Johnson, E.A. Hinds, F.M.J. Pichanick, Phys. Rev. A 32 (1985) 2712.
[20] Ping Zhao, J.R. Lawall, F.M. Pipkin, Phys. Rev. Lett. 66 (1991) 592.
[21] W. Happer, Rev. of. Modern Phys. 44 (2) (1972) 169.
[22] Bouchiat et al., Phys. Rev. Lett. 5 (8) (1960) 373.
[23] L.D. Schearer, F.D. Colegrove, G.K. Walters, Phys. Rev. 132 (6) (1963) 2561.
[24] C.G. Aminoff, C. Larat, M. Leduc, F. Laloë, Revue Phys. Appl. 24 (1989) 827.
[25] F.D. Colegrove, P.A. Franken, Phys. Rev. 119 (2) (1960) 680.
[26] Eckert et al., Nucl. Instr. and Meth. A 320 (1992) 53.
[27] K. Lee, J.-O. Hansen, J.F.J. van den Brand, R.G. Milner, Nucl. Instr. and Meth. A 333 (1993) 294.
[28] D. DeSchepper et al., Nucl. Instr. and Meth. A 419 (1998) 16.
[29] J.M. Daniels, R.S. Timsit, Can. J. Phys. 49 (1971) 525.
[30] D.S. Betts, M. Leduc, Ann. Phys. Fr. 11 (1986) 267.
[31] J. Dupont-Roc, M. Leduc, F. Laloë, Phys. Rev. Lett. 27 (8) (1971) 467.
[32] D.A. Landmann, Bull. Am. Phys. Soc. 12 (1967) 94.
[33] L.D. Schearer, Phys. Rev. 160 (1) (1967) 76.
[34] R.B. Partridge, G.W. Series, Proc. Phys. Soc. 88 (1966) 983.
[35] P.J. Nacher, M. Leduc, J. Phys. (Paris) 46 (1985) 2057.
[36] J. Dupont-Roc, M. Leduc, F. Laloë, J. Phys. (Paris) 34 (1973) 961.
[37] R.L. Gamblin, T.R. Carver, Phys. Rev. 138 (4A) (1965) A946.
[38] L.D. Schearer, G.K. Walters, Phys. Rev. 139 (5A) (1965) A1398.
[39] R.S. Timsit, J.M. Daniels, A.D. May, Can. J. Phys. 49 (1971) 560.
[40] C.E. Jones et al., Phys. Rev. C 47 (1) (1993) 110.
[41] W. Heil, Phys. Lett. A 201 (1995) 337.
[42] T.R. Gentile, R.D. McKeown, Phys. Rev. A 47 (1) (1993) 456.
[43] M. Leduc, P.J. Nacher, F. Lalö, J.M. Daniels, Helvetica Phys. Acta 59 (1986) 747.
[44] Bagdasarov et al., Sov. J. Quantum Electron. 13 (8) (1983) 1082.
[45] C.G. Aminoff, S. Essabaa, I. Brissaud, J. Arianer, Opt. Commun. 86 (1991) 99.
[46] Kahn et al., J. Appl. Phys. 52 (11) (1981) 6864.

[47] A. Roth, Vacuum Technology, North-Holland Publishing Company, 1976, ISBN 0-7204-0313 #8.
[48] Z.-L. Zhou, Ph.D. Thesis, University of Wisconsin, Madison, USA, 1996.
[49] O. Unal, Ph.D. Thesis, University of Wisconsin, Madison, USA, 1995.
[50] O. Postma, NIKHEF Internal Report, MT 96-3, 1996.
[51] M. Pavlović, F. Lalöe, J. Phys. France 31 (1970) 173.
[52] F. Lalöe, Ann. Phys. (Paris) 6 (1971) 5.
[53] Bigelow et al., J. Phys. II France 2 (1992) 2159.
[54] W. Lorenzon, T.R. Gentile, H. Gao, R.D. McKeown, Phys. Rev. A 47 (1) (1993) 468.